

The impact of Greenland melt on local sea levels: a partially coupled analysis of dynamic and static equilibrium effects in idealized water-hosing experiments

A letter

Robert E. Kopp · Jerry X. Mitrovica ·

Stephen M. Griffies · Jianjun Yin ·

Carling C. Hay · Ronald J. Stouffer

Submitted: 6 June 2010 / Accepted: 14 August 2010 / Authors' version: 13 September 2010
This is the authors' version of the article.

The final publication is available at www.springerlink.com

Abstract Local sea level can deviate from mean global sea level because of both dynamic sea level (DSL) effects, resulting from oceanic and atmospheric circulation and temperature and salinity distributions, and changes in the static equilibrium (SE) sea level configuration, produced by the gravitational, elastic, and rotational effects of mass redistribution. Both effects will contribute to future sea level change. To compare their magnitude, we simulated the effects of Greenland Ice Sheet (GIS) melt by conducting idealized North Atlantic “water-hosing” experiments in a climate model unidirectionally coupled to a SE sea level model. At current rates of GIS melt, we find that geographic SE patterns should be challenging but possible to detect above dynamic variability. At higher melt rates, we find that DSL trends are strongest in the western North Atlantic, while SE effects will dominate in most of the ocean when melt exceeds ~20 cm equivalent sea level.

R. E. Kopp

Department of Geosciences and Woodrow Wilson School of Public and International Affairs,
Princeton University, Princeton, NJ 08544, USA, and AAAS Science & Technology Policy
Fellow, American Association for the Advancement of Science, Washington, DC 20005, USA.
E-mail: rkopp@alumni.caltech.edu

J. X. Mitrovica

Department of Earth and Planetary Sciences, Harvard University, Cambridge, MA 02138,
USA

S. M. Griffies and R. J. Stouffer

Geophysical Fluid Dynamics Laboratory, National Oceanic and Atmospheric Administration,
Princeton, NJ 08542, USA.

J. Yin

Center for Ocean-Atmospheric Prediction Studies, Florida State University, Tallahassee, FL
32306, USA.

C. C. Hay

Department of Physics, University of Toronto, Toronto, ON M5S 1A7, Canada.

1 Introduction

Global sea level (GSL) rise and local sea level (LSL) change are prominent consequences of global warming. Both thermal expansion and melting grounded ice increase ocean volume and thus GSL, which is defined as the area-weighted mean of sea level over the ocean. LSL changes differ from GSL rise due to three major processes: dynamic sea level (DSL) effects, changes in the static equilibrium (SE) sea level configuration caused by ocean and cryosphere mass redistribution, and local land movements and gravity perturbations due to factors such as tectonics and hydrology. (The last are generally unrelated to climate change and beyond the scope of this paper.)

Sea surface height (SSH) corresponds to a gravitational equipotential surface and is measured relative to a reference ellipsoid; sea level refers to the elevation of the sea surface above the sea bottom (Fig. 1a). DSL changes, which affect sea surface height, include changes in ocean volume distribution caused by shifting ocean or atmospheric circulation and by local thermosteric effects (Gregory et al., 2001). SE sea level changes are driven by surface mass redistributions, which (1) directly perturb the gravitational field of the Earth and thus SSH, (2) deform the solid sea bottom (also further perturbing the gravitational field and SSH), and (3) shift both the sea bottom and the sea surface by changing the orientation and rate of planetary rotation (Kendall et al., 2005). Notably, SE sea level initially falls near a rapidly melting ice sheet due to the loss of gravitational attraction and crustal deflection, as mass that was concentrated in the ice sheet is redistributed more diffusely through the ocean, and it rises faster than GSL far from it (Mitrovica et al., 2001) (Figs. 1a-b, S1). Over subsequent millennia, mantle flow isostatically compensates for the displaced mass, gradually counterbalancing these initial effects.

Dynamic and SE sea level are studied by two different subdisciplines – climate modeling and glacial rebound modeling – and to date, projections that attempt to combine both (e.g., Katsman et al., 2008) have been scarce. In this paper, we jointly examine DSL and SE effects of idealized Greenland Ice Sheet (GIS) melt. We consider the relative magnitude over time of these effects both for low rates of melt, comparable to the present level of ~0.3 mm equivalent sea level (esl)/y (Shepherd and Wingham, 2007), and for high rates of melt (0.1 Sv, equivalent to 8.7 mm esl/y). The latter value is somewhat higher than but comparable to projections of physically plausible twenty-first century GIS melt rates (~60 cm/century; Pfeffer et al., 2008). (In the Supplemental Material, we also consider a 1.0 Sv sensitivity test.) These analyses are intended to be illustrative; they focus on an idealized representation of one major factor contributing to sea level rise, GIS melt, while neglecting other meltwater sources and thermal expansion.

For low melt rates, freshwater hosing experiments in fully coupled atmosphere-ocean general circulation models (AOGCMs) do not yield clear DSL trends but do generate DSL variability. We examine the challenge that DSL variability, as modeled in the absence of melt, poses for detecting geographic patterns in SE trends. For high melt rates, we approximate GIS melting in the AOGCM

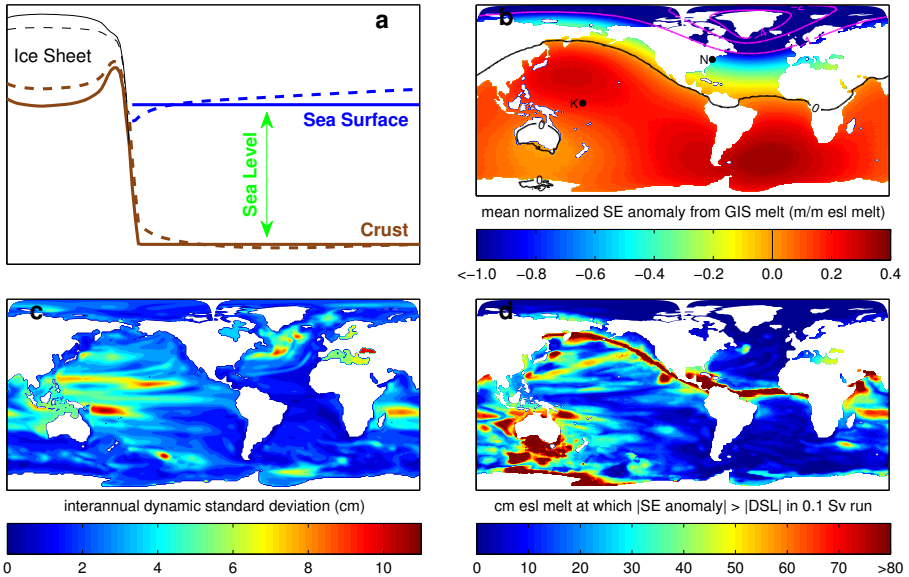


Fig. 1 **a** Schematic illustration of SE sea level change. Sea level (*green arrow*) is defined as the height of the sea surface (*blue*) above the sea bottom (*brown*). *Dotted lines* illustrate the change in sea surface and sea bottom altitude initially caused by a rapidly melting ice sheet. **b** Mean change in SE LSL anomaly per meter esl lost from GIS. *Black contours* mark 0 m; *magenta* marks -1 , -2 , and -4 m. At -1 m, the SE LSL anomaly is sufficient to cancel GSL rise. **c** DSL variability indicated by interannual standard deviation in the zero-hosing run. **d** Level of total melt at which the amplitude of the SE LSL anomaly first begins to exceed the amplitude of the DSL anomaly in the 0.1 Sv run. The white triangular masked regions in the north are plotting artifacts arising from the non-spherical Arctic Ocean coordinate grid.

by freshwater hosing of the North Atlantic. SE sea level changes are calculated based on uniform GIS mass loss plus the modeled ocean and sea-ice mass distributions and are added to the modeled DSL changes to yield total sea level change. These approaches provide both the first direct global comparison of DSL and SE effects and the first SE calculations to include dynamic ocean mass distribution.

2 Methods

We employed the GFDL CM 2.1 climate model with the MOM4.0 ocean code (Delworth et al, 2006; Griffies et al, 2005). Radiative forcing was kept constant at 1860 levels. In the hosing runs, following the CMIP coordinated experiment protocol (Stouffer et al, 2006), an external freshwater flux was added uniformly to the surface of the North Atlantic between 50°N and 70°N during years 1–100; years 101–200 followed the end of the hosing. We measure DSL changes through the effective sea surface height (SSH), defined as the sum of the prognostic free surface height plus the additional height of sea water that would

be produced by melting all sea-ice. The mass distribution of liquid sea water plus solid sea-ice for each time step was calculated from AOGCM output as described in the Supplemental Material.

For analyses employing the zero-hosing run, we use standard SE sea level patterns calculated without coupling to the AOGCM (Mitrovica et al, 2001). For other analyses, the combined ocean–sea-ice–land-ice mass redistributions were calculated by assuming that any net change in ocean and sea-ice mass was compensated by a geographically uniform ice mass flux over Greenland. These mass redistributions were passed to a pseudo-spectral algorithm for solving the SE sea level equation (Kendall et al, 2005). This algorithm, which included gravitational, deformational and rotational effects on sea level, yields a mass-conserving perturbation to the SE sea level configuration.

As used herein, “LSL anomaly” refers to the deviation at each time step of LSL from GSL.

3 Static equilibrium sea level “fingerprint” detection above dynamic variability at low melt rates

Because individual ice sheets produce distinct “fingerprints” in the SE sea level configuration (Mitrovica et al, 2001), geographically distributed sea level measurements can be used to estimate the individual contributions from different meltwater sources, complementing local altimetry measurements of ice elevation and satellite observations of regional gravity changes. At low melt rates, however, SE trends can be obscured by DSL variability.

We estimate detection thresholds for GIS melt by comparing, within a linear least-squares framework, interannual DSL variability in the zero-hosing run to SE effects due to different GIS melt rates (Fig. 1b-c and Supplemental Material). In this context, we define a detection threshold as the melt rate at which it is possible to identify net GIS mass loss with 95% confidence. The derived detection thresholds are approximate lower bounds, because they do not include confounding sea level trends, such as those due to thermal expansion, Antarctic melt or glacier melt, and are based upon modeled DSL variability, which is $\sim 20\%$ less than observed variability (Fig. S2). They provide an initial estimate of the feasibility of detection given available data.

We consider two different types of observations: tide gauges and satellite altimetry (Fig. S3). Tide gauges are a primary source of sea level observations and have existed for considerably longer than alternative instruments. They can thus serve as a key data source for inferring twentieth-century ice sheet mass changes. A realistic network of 150 tide gauges spanning the 370 cm/m SE anomaly range covered by the current global network could detect ~ 0.8 mm esl/y GIS melt in ~ 20 years, ~ 0.2 mm esl/y melt in ~ 50 years and ~ 0.07 mm esl/y melt in a century.

Since the launch of Geosat in 1985, satellite altimetry of SSH has provided more geographically-widespread constraints on one of the bounding surfaces that define sea level. However, because SSH fingerprints are somewhat lower

in amplitude than sea level fingerprints (Fig. S1), the sensitivity enhancement resulting from the geographic span is limited. We estimate that regular satellite measurements of SSH within 66° of the equator, as currently provided by the Jason satellites, could detect 0.7 mm esl/y GIS melt in ~ 20 years, 0.3 mm esl/y in ~ 35 years and 0.2 mm esl/y in ~ 50 years.

Estimates of the rate of GIS melt loss over the last ~ 2 decades range from -11 to 227 Gt/y (0.0–0.6 mm esl/y) (Shepherd and Wingham, 2007). The median estimate is comparable to the detection thresholds for ~ 40 years of tide gauge and ~ 35 years of altimetry data. It should therefore be challenging but feasible to detect the SE signal of GIS melt in these records (Mitrovica et al, 2001). Accelerated melt rates of $\sim 2\text{--}6$ mm esl/y (Pfeffer et al, 2008) should be detectable above background DSL variability within less than a decade of their onset.

4 Combined dynamic and static trends at high melt rates

At higher melt rates, AOGCMs yield clear DSL trends as well as DSL variability analogous to that observed at low melt rates. Consistent with prior work on the DSL effects of a slowing Atlantic meridional overturning circulation (AMOC) (Yin et al, 2009) and with other recent models of the effect of Greenland melting on DSL (Stammer, 2008; Hu et al, 2009), the 0.1 Sv water-hosing run gives rise to a strong west-to-east gradient in the North Atlantic (Fig. 2a-b), with particularly strong DSL rise along the northeast coast of the United States. No comparably strong anomalies are observed in the rest of the ocean.

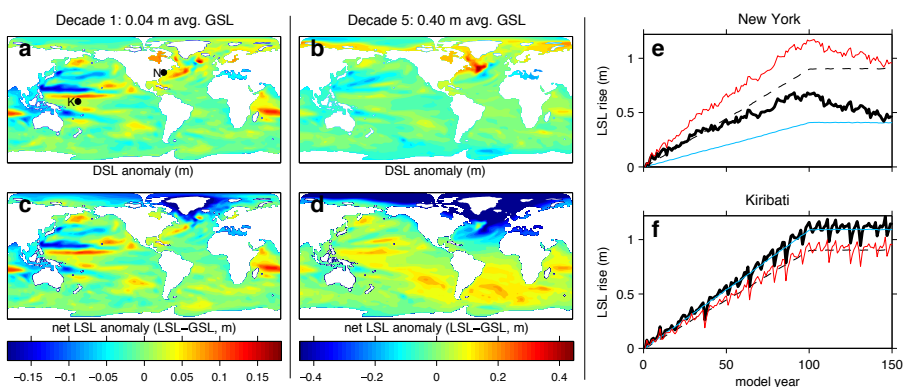


Fig. 2 (a, b) Maps of DSL anomaly and (c, d) net dynamic plus SE LSL anomaly averaged over the (a, c) first and (b, d,) fifth decades of the 0.1 Sv run. Note scale change between (a, c) and (b, d). “LSL anomaly” is the difference between LSL and GSL. (e, f) GSL rise (black dashed) and LSL rise including dynamic (red), SE (blue) or both dynamic and SE effects (black solid) at (e) New York City (*N*) and (f) Kiribati (*K*). The locations of *N* and *K* are marked in (a). The freshwater hosing occurs in years 0–100, then stops.

In both the 0.1 and 1.0 Sv runs, dynamic effects tend to quasi-asymptotically approach some value associated with melt rate, while SE effects are almost exactly linear with total melt (Figs. 2e-f, S4). As a consequence, in the 0.1 Sv run, SE effects become dominant over dynamic effects in 25% of the ocean after ~ 8 cm esl melt (~ 9 years), in 50% of the ocean after ~ 18 cm esl melt (~ 21 years), and in 75% of the ocean after ~ 33 cm esl melt (~ 38 years) (Figs. 1d, 2c-d, S5, S6).

LSL anomaly curves from two localities of particular interest – New York City (NYC), which is in the northwestern Atlantic region that experiences the strongest dynamical effects, and Kiribati, a representative South Pacific island distal to the GIS – illustrate the contributions of dynamic and SE effects (Fig. 1b, 2).

NYC experiences a growing DSL anomaly that climbs roughly asymptotically to 26–31 cm over a century of hosing, then relaxes to zero over the half-century following the end of the hosing. However, the SE anomaly associated with GIS melting counteracts almost all the dynamic anomaly; the decadal average net LSL anomaly is 2–3 cm for the first four decades (as GIS melt climbs to ~ 35 cm esl) then becomes increasingly negative, so LSL is first marginally above GSL then falls below it.

Kiribati experiences significant interannual DSL oscillations but no sustained DSL trend. The decadal mean DSL anomaly oscillates between -3 and +3 cm through the experiment. Kiribati does, however, experience a significant positive SE LSL anomaly; after the first century, the net LSL anomaly is about 20 cm.

5 Discussion and Conclusions

Our combined analysis emphasizes the need for geophysicists working on the effects of ice sheet melt to include DSL effects in their considerations and for climate modelers to consider SE effects in their calculations.

At current estimated melt rates, the SE effects of ice sheet mass loss lie near the detection thresholds of the available records. Combining these records with statistically robust methods thus offers the best chance of recognizing SE fingerprints over DSL variability.

At accelerated melt rates, both DSL and SE trends are significant and need to be examined jointly. DSL trends will likely dominate initially in most of the ocean, with SE effects coming to dominate in much of the ocean as total loss reaches the decimeter esl (a few 10^4 Gt) scale. While SE effects will dominate most quickly near melting ice sheets, projections in these regions suffer from two important limitations. First, the DSL perturbation will be largest near a meltwater source, but is poorly characterized in our idealized representation of GIS melting, which spreads freshwater evenly over a large area of the North Atlantic. Second, the precise pattern of SE sea level in this region is sensitive to the detailed melt geometry.

Regardless of melt rate, the LSL anomaly off the northeastern United States will likely be strongly influenced by a DSL rise caused by slowing of AMOC. GIS melting will contribute to this slowing, though its effect will be damped by SE effects. High-latitude ocean warming and increased net precipitation will also contribute, and without any similar dampening (Yin et al., 2009). This region is therefore a challenging area in which to look for the SE fingerprint of GIS melting, but a key region in which to look for the effects of AMOC slowing (Bingham and Hughes, 2009). Our results suggest that dynamic effects may play an important role in explaining the north-south sea level rise gradient observed in regional tide gauge records (Douglas, 1991).

In this analysis, we let dynamic ocean mass distribution affect SE sea level but assume that no feedback exists between changes in SE and ocean circulation. We therefore calculate net LSL anomalies by adding DSL and SE anomalies. Because SE effects operate on a longer wavelength than most dynamic effects, this assumption is likely correct. However, the possibility that horizontal gravitational anomalies near a melting ice sheet could deflect descending water masses and thereby alter ocean circulation is worthy of investigation.

The North Atlantic hosing we employ is only a first-order approximation to GIS melt. Avenues for future work include modeling meltwater from GIS, as well as from the West Antarctic Ice Sheet (WAIS), with more realistic geographic and depth distributions. Realistic combinations of anthropogenic warming (e.g., Yin et al., 2009) (absent here) with ice sheet melt should also be considered. Because both GIS melting and ocean warming weaken the AMOC, we do not expect the associated LSL anomalies to add linearly. Finally, reducing discrepancies in DSL among different climate models (Yin et al., 2009) is necessary for reliable projections of LSL patterns associated with ocean warming and melting ice sheets.

Acknowledgements We thank K. Bryan, F. Simons, R. Hallberg, M. Oppenheimer, J. Wahr, M. Winton and an anonymous reviewer for helpful discussion. REK was supported by a postdoctoral fellowship in the Science, Technology, and Environmental Policy program at the Woodrow Wilson School at Princeton University and by an appointment to the US Department of Energy American Association for the Advancement of Science Fellowship Program administered by Oak Ridge Institute for Science and Education.

References

- Bingham RJ, Hughes CW (2009) Signature of the Atlantic meridional overturning circulation in sea level along the east coast of North America. *Geophys. Res. Lett.* 36:L02603, doi:10.1029/2008GL036215
- Delworth TL et al. (2006) GFDL's CM2 global coupled climate models - Part 1: Formulation and simulation characteristics. *J. Climate* 19:643–674
- Douglas BC (1991) Global sea level rise. *J. Geophys. Res.* 96:6981–6992, doi:10.1029/91JC00064
- Gregory J et al. (2001) Comparison of results from several AOGCMs for global and regional sea-level change 1900–2100. *Clim. Dyn.* 18:225–240
- Griffies SM et al. (2005) Formulation of an ocean model for global climate simulations. *Ocean Sci.* 1:45–79

- Hu A et al. (2009) Transient response of the MOC and climate to potential melting of the Greenland Ice Sheet in the 21st century. *Geophys. Res. Lett.* 36:L10707, doi:10.1029/2009GL037998
- Katsman C et al. (2008) Climate scenarios of sea level rise for the northeast atlantic ocean: a study including the effects of ocean dynamics and gravity changes induced by ice melt. *Climatic Change* 91:351–374
- Kendall R, Mitrovica J, Milne G (2005) On post-glacial sea level – II. Numerical formulation and comparative results on spherically symmetric models. *Geophys. J. Int.* 161:679–706
- Mitrovica JX et al. (2001) Recent mass balance of polar ice sheets inferred from patterns of global sea-level change. *Nature* 409:1026–1029
- Pfeffer WT, Harper JT, O'Neal S (2008) Kinematic constraints on glacier contributions to 21st-century sea-level rise. *Science* 321:1340–1344
- Shepherd A, Wingham D (2007) Recent sea-level contributions of the antarctic and greenland ice sheets. *Science* 315:1529–1532
- Stammer D (2008) Response of the global ocean to greenland and antarctic ice melting. *J. Geophys. Res.* 113:C06022, doi:10.1029/2006JC004079
- Stouffer RJ et al. (2006) Investigating the causes of the response of the thermohaline circulation to past and future climate changes. *J. Climate* 19:1365–1387
- Yin J, Schlesinger ME, Stouffer RJ (2009) Model projections of rapid sea-level rise on the northeast coast of the United States. *Nat. Geosci.* 2:262–266

**SUPPLEMENTAL MATERIAL TO “THE IMPACT OF GREENLAND MELT ON
LOCAL SEA LEVELS: A PARTIALLY COUPLED ANALYSIS OF DYNAMIC AND
STATIC EQUILIBRIUM EFFECTS IN IDEALIZED WATER-HOSING
EXPERIMENTS”**

ROBERT E. KOPP, JERRY X. MITROVICA, STEPHEN M. GRIFFIES, JIANJUN YIN, CARLING C. HAY,
AND RONALD J. STOUFFER

SUPPLEMENTAL METHODS

Climate model. For each experiment, the climate model was spun up for several centuries before the start of hosing. To remove baseline values and model drift, we found the least-squares linear fit over time to SSH and column mass at each grid cell in the zero-hosing run and subtracted the fitted values from the output of all runs. GSL is calculated as the area-weighted mean of SSH plus a small correction term (see below) added because Boussinesq models do not explicitly compute global steric sea level changes.

Sea level model. In contrast to conventional solutions to the SE sea level equation, which use ice mass changes as input, our analysis uses the total ocean-cryosphere mass redistribution. Solutions were truncated at spherical harmonic degree and order 512. Since the time scale we are considering is short relative to the Maxwell time of the planet, the calculations treat the Earth model as purely elastic (i.e., the SE response is instantaneous, with no viscous memory). We used the elastic and density structure of the Earth from the seismic model PREM (Dziewonski and Anderson, 1981).

Mass distribution. In each model run, the distribution of liquid seawater mass plus solid sea ice mass was calculated from the seawater density ρ and SSH output according to

$$(S1) \quad m(x, y) = \sum_z^{\text{water column}} \rho(x, y, z) dV(x, y, z) + I(x, y) - \frac{dA(x, y)}{A} \tilde{m}.$$

In this equation, dV is the volume of a liquid ocean grid cell (including changes associated with the ocean free surface), the sum is over a vertical column of liquid seawater from the ocean bottom to surface, I is sea ice mass, and dA/A is the fraction of global ocean surface area at each grid cell.

The term \tilde{m} is a globally uniform correction to the seawater mass arising from the use of a mass-nonconserving Boussinesq ocean model (Greatbatch, 1994; Bryan, 1997; Ponte, 1999). It is equal to zero in the initial time step and is given at time step t_N ($N > 1$) by

$$(S2) \quad \tilde{m}(t_N) = \sum_{n=2}^N \Delta \tilde{m}_n$$

$$(S3) \quad \Delta \tilde{m}_n = [\bar{\rho}(t_n) - \bar{\rho}(t_{n-1})] V(t_n)$$

where $\bar{\rho}(t)$ and $V(t)$ are respectively the global mean ocean density and the total ocean volume at time t . In the hosing experiments, both the term \tilde{m} and the sea level correction term $\text{SSH}^{\text{steric}}$ described below amount to no more than a few percent of the uncorrected global mean mass change and sea level change.

Steric sea level correction term. Boussinesq models do not explicitly compute global steric sea level changes. We therefore compute a globally-uniform steric correction term for SSH given at time t_N by

$$(S4) \quad \text{SSH}^{\text{steric}}(t_N) = \frac{1}{A} \sum_{n=2}^N -\frac{\Delta \tilde{m}_n}{\bar{\rho}(t_n)},$$

where A is the global ocean surface area.

Comments on virtual salt flux and Boussinesq approximations. We note that the virtual salt flux approximation (VSF) commonly employed in ocean models does not provide a straightforward way to account for mass effects. Instead of directly treating a freshwater flux (FWF) into the ocean, VSF treats freshwater input as a negative salt flux while keeping the ocean mass constant. Models employing VSF do a reasonable job of calculating DSL anomalies (Yin et al., 2010; Stammer, 2008; Hu et al., 2009) but require exogenous treatment of GSL rise. Mass redistribution can be calculated simply in a FWF model, as in our analysis, but VSF models will require some ad hoc technique to do so. Additionally, the volume-conserving Boussinesq approximation commonly used in ocean models is awkward conceptually and quantitatively. We therefore recommend that future ocean models, especially those coupled to gravity calculations, should employ a mass-conserving non-Boussinesq formulation.

INTERANNUAL VARIABILITY: ZERO-HOSING RUN VERSUS OBSERVATIONS

We have compared the interannual sea level variability in the zero-hosing run with the variability observed in detrended records from the 1166 widely distributed sites within the RLR tide gauge data set of the Permanent Service for Mean Sea Level (PSMSL; www.pol.ac.uk/pmsl). The ratio of the observed to zero-hosing run standard deviation at a subset of 657 sites (chosen because of climate model resolution) is shown in Fig. S2. The inter-site mean standard deviation for the zero-hosing run and the tide gauge records are 3.25 cm and 3.60 cm, respectively, while the mean ratio of the tide gauge standard deviation to the zero-hosing run standard deviation is 1.26.

There are many reasons for the difference between the variability in the climate model and the observations. One reason is model limitations. The climate model is run at a relatively coarse resolution (1 deg). There are many coastal processes either poorly simulated or not simulated at all. Many of these processes (but not all) influence sea level on time scales shorter than 1 year. Another model limitation is that the simulation of variability may not be realistic. For example, it is well known that this model simulates too large ENSO variability in the tropical Pacific Ocean (Wittenberg et al., 2006).

Moreover, in this model integration, the radiative forcing is held constant at 1860 values, whereas in the observations, the radiative forcing is changing due to solar activity, volcanic eruptions, and anthropogenic forcings. Volcanoes in particular can produce natural changes in sea level that persist for many decades (Delworth et al., 2005; Gleckler et al., 2006). These three issues make the model-observation comparison difficult and are some of the reasons why the estimates of trend detection times are likely lower bounds.

DETECTING A SEA LEVEL ANOMALY TREND ABOVE BACKGROUND VARIABILITY

Attempts to identify static equilibrium (SE) sea level trends must take into account background dynamic variability of the magnitude shown in Figure 1a.

Consider two global sea level trends: one from effects independent of ice sheet melt of rate g , and one from a single ice sheet of rate h . At site i and time t , sea level is given by

$$(S5) \quad z_i(t) = z_i(0) + gt + h(1 + k_i)t + \epsilon_i(t),$$

where k_i is the normalized SE anomaly at site i due to the melting ice sheet and $\epsilon_i(t)$ is background dynamic sea level variability. This expression can be rewritten in matrix notation as

$$(S6) \quad \Delta \mathbf{z} = \mathbf{X} \mathbf{a} + \mathbf{e}.$$

For m sites observed at n times, $\Delta \mathbf{z}$ is the $mn \times 1$ column vector of observations, ordered such that the elements $(i-1) \cdot n + 1$ to in correspond to the n observations at site i . The value of the observations at the first time point are all set to zero. \mathbf{X} is the $mn \times 2$ matrix in which the first column, reflecting the

weight of the non-ice sheet related global sea level trend, is equal to the value of t for the observation and the second column is equal to the value of $(1 + k_i)t$ for the observation. \mathbf{a} is a 2×1 row vector [$g\ h$], and the $mn \times 1$ column vector \mathbf{e} records the background variability for each observation. \mathbf{e} is normally distributed with mean $\mathbf{0}$ and covariance \mathbf{V} .

We find the least-squares fit of the observed values of $\Delta\mathbf{z}$ to the linear model

$$(S7) \quad \Delta\mathbf{z} = \mathbf{X}\hat{\mathbf{a}}$$

where $\hat{\mathbf{a}} = [\hat{g}\ \hat{h}]$. The mean value of $\hat{\mathbf{a}}$ is equal to \mathbf{a} . Its estimated covariance \mathbf{M} is given by the 2×2 matrix

$$(S8) \quad \mathbf{M} = (\mathbf{X}^\top \mathbf{X})^{-1} \mathbf{X}^\top \mathbf{V} \mathbf{X} (\mathbf{X}^\top \mathbf{X})^{-1}.$$

The second element of the second row of \mathbf{M} is the estimated variance of \hat{h} , which we denote σ^2 . We define the 95% confidence detection threshold for ice sheet melt as the value of h at which there is an estimated 95% probability that $\hat{h} > 0$. We note that $\hat{h} > 0$ is distributed according to Student's t distribution with $mn - m - 2$ degrees of freedom; for large values of mn , the detection threshold is given by 1.65σ .

We compute detection thresholds for two different measurement instruments: tide gauges and satellite altimetry (Fig. S3). For each calculation, we characterize \mathbf{V} using the output of the zero-hosing run. For the tide gauges, we use output at 150 sites, taken (due to computation limitations) as a subset of the 1166 tide gauge sites in the PSMSL database. Because detection thresholds are extremely sensitive to the range of normalized SE anomalies covered, in taking the subset, we sampled evenly through the different normalized anomalies present in the data set while preserving both the maximum and minimum values. For satellite altimetry, we use output averaged across 150 equal-area sectors within 66° of the equator (such as might be observed by a satellite with an orbital inclination of 66° , such as Jason or Jason-2). Detection thresholds for each of the observation networks are shown as a function of record length in Figure 1c. Note that the relevant SE fingerprint for tide gauges reflects changes in sea level, while that for satellite altimetry data reflects changes in sea surface height (Fig. S1).

To examine detection threshold sensitivities, we also consider the idealized case of observations at sites at which interannual variability is uncorrelated and between which no correlation of variability exists. Results from this simple statistical analysis, assuming $\sigma = 3.1$ cm as in the area-weighted mean value from the zero-hosing run, are shown in Fig. S7. Fig. S7a shows detection thresholds (in terms of mm esl melt/y) with 20 years of data, different ranges of normalized SE anomaly, and different densities of sites evenly distributed within the anomaly range. Fig. S7b shows detection thresholds with 10 sites, different ranges of normalized SE anomaly, and varying numbers of years of data.

Detection thresholds are sensitive to record duration, the range of the normalized SE anomaly spanned by the observation network, and the density of the network. Increasing any of these parameters reduces the detection threshold. A typical SE anomaly has a magnitude of about 30 cm/m (Fig. S7b), the area-weighted mean absolute value. For an idealized network consisting of two points with anomalies of ± 30 cm/m, at which interannual variability with a standard deviation of 3.1 cm is uncorrelated year-to-year and between sites, it would require ~ 20 years of data to detect 2.5 mm esl/y GIS melt and ~ 50 years for 0.6 mm esl/y. A 100-site network spanning the same range would detect 0.1 mm esl/y of melt in ~ 50 years. Expanding the range of the SE anomaly sampled by the network yields greater benefits; a two-site network with a SE anomaly range spanning from -340 cm/m to $+30$ cm/m (the range covered by the current global tide gauge network) could detect 0.09 mm esl/y melt with ~ 50 years of data, while a 100-site network with the same range could detect 0.02 mm esl/y melt in the same period.

SENSITIVITY ANALYSIS WITH 1.0 SV RUN

The 1.0 Sv run, which corresponds to the addition of 8.7 m esl over one century, is physically impossible with respect to GIS, which contains only ~ 7 m esl of ice, but serves to investigate the sensitivity of DSL to melt rate.

In this run, a strong DSL anomaly occurs across the North Atlantic and through much of the Arctic Ocean (Fig. S5). No comparably strong anomalies are observed in the rest of the ocean. This result is consistent with other recent models of the effect of Greenland melting on DSL (Stammer, 2008; Hu et al,

2009). SE effects dominate in the first year of the experiment (\sim 0–9 cm esl melt) in 38% of the ocean, in 50% of the ocean after 2 years (\sim 9–17 cm esl melt), and in 75% of the ocean after 6 years (\sim 44–52 cm esl melt). In both the 0.1 and 1.0 Sv experiments, DSL remains dominant into the second century in approximately 4% of the ocean (Fig. S6).

At New York City (NYC; Fig. S4), the nonlinearity of the DSL trend is more pronounced in the 1.0 Sv run than in the 0.1 Sv run; the DSL anomaly reaches 0.9 m by the third decade and peaks at 1.2 m at the end of the first century. Its decay is more protracted; at the end of the second century, the DSL anomaly is still 0.6 m. However, the linear effects of SE overpower sub-linear dynamic effects; the net LSL anomaly in NYC peaks at 9–12 cm during years 7–16 (when ice sheet melt is 0.5–1.3 m esl) and then declines, becoming negative in year 21 (when ice sheet melt reaches 1.8 m esl).

While in the 0.1 Sv Kiribati experiences no secular DSL anomaly, in the 1.0 Sv run, it experiences a slight negative DSL anomaly, which reaches a minimum value of -0.2 m. This dynamic effect is strongly outweighed by SE effects; the net LSL anomaly reaches 1.7 m at the end of the first century and 1.9 m at the end of the second century.

In addition to NYC and Kiribati, we also examined LSL anomaly curves for the sensitivity analysis at Bermuda, a north Atlantic site commonly referenced in paleo-sea level studies that is less exposed to dynamic effects in the 0.1 Sv run than NYC. In the 0.1 Sv run, Bermuda experiences a minimal positive DSL anomaly, with a decadal mean value of 1 to 5 cm through most of the first century of the experiment. This DSL anomaly is overwhelmed by SE effects, so that the net LSL anomaly reaches -30 cm at the end of the first century (with ice sheet melt of 0.87 m esl). In contrast, in the 1.0 Sv run, Bermuda experiences a positive DSL anomaly that peaks at 0.7 m. As in NYC, this positive DSL anomaly is overpowered by the negative SE anomaly, such that the net LSL anomaly is always negative.

REFERENCES

- Bryan FO (1997) The axial angular momentum balance of a global ocean general circulation model. *Dynamics of Atmospheres and Oceans* 25:191–216
- Delworth TL, Ramaswamy V, Stenchikov G (2005) The impact of aerosols on simulated ocean temperature and heat content in the 20th century. *Geophys. Res. Lett.* 32:L24709, doi:10.1029/2005GL024457
- Dziewonski A, Anderson D (1981) Preliminary reference Earth model. *Phys. Earth Planet. Inter.* 25:297–356
- Gleckler PJ, Achuta-Rao K, Gregory JM, Santer BD, Taylor KE, Wigley T (2006) The effect of volcanic eruptions on ocean heat content and thermal expansion. *Geophys. Res. Lett.* 33:L17702, doi:10.1029/2006GL026771
- Greatbatch RJ (1994) A note on the representation of steric sea level in models that conserve volume rather than mass. *J. Geophys. Res.* 99:12,767–12,771
- Hu A, Meehl GA, Han W, Yin J (2009) Transient response of the MOC and climate to potential melting of the Greenland Ice Sheet in the 21st century. *Geophys. Res. Lett.* 36:L10707, doi:10.1029/2009GL037998
- Ponte RM (1999) A preliminary model study of the large-scale seasonal cycle in bottom pressure over the global ocean. *J. Geophys. Res.* 104:1289–1300
- Stammer D (2008) Response of the global ocean to greenland and antarctic ice melting. *J. Geophys. Res.* 113:C06022, doi:10.1029/2006JC004079
- Wittenberg AT, Rosati A, Lau NC, Poshay JJ (2006) GFDL's CM2 Global Coupled Climate Models. Part III: Tropical Pacific Climate and ENSO. *J. Climate* 19:698–722
- Yin J, Stouffer RJ, Spelman MJ, Griffies SM (2010) Evaluating the uncertainty introduced by the virtual salt flux assumption in climate simulations and future projections. *J. Climate* 23:80–96

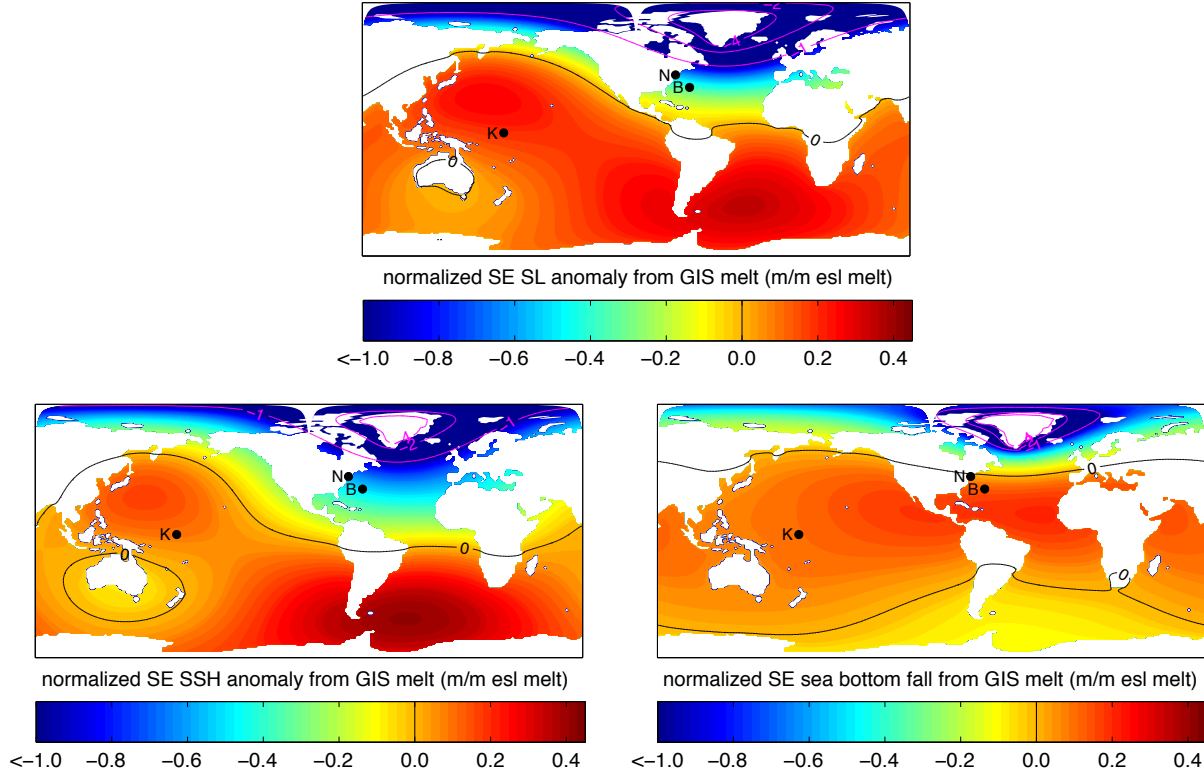


FIGURE S1. Change in SE sea level anomaly per meter esl lost from GIS (top) is equal to the sum of an increase in SSH (bottom left) and a decrease in the altitude of the sea bottom (bottom right). Distributions shown are standard patterns calculated without coupling to the AOGCM. Black contours mark 0 m; grey contours mark -1, -2, and -4 m. At -1 m, the local SE sea level anomaly is sufficient to cancel global mean rise. The locations of New York City (N), Bermuda (B) and Kiribati (K) are marked.

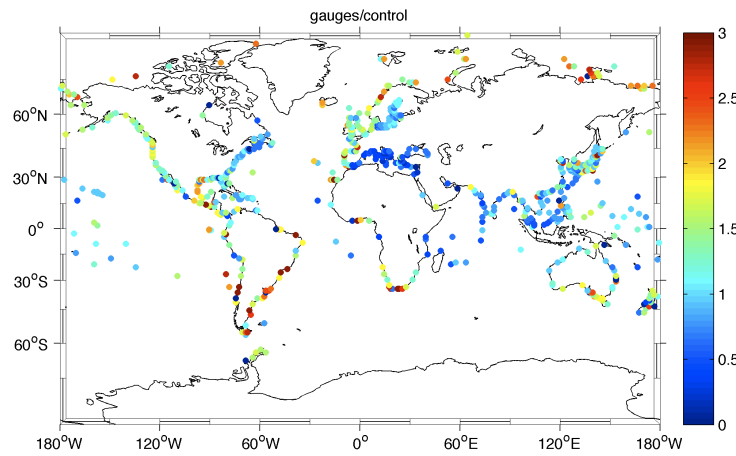


FIGURE S2. The ratio of the standard deviation of detrended observational sea level data to zero-hosing run data at all 657 sites within the RLR tide gauge data set of the Permanent Service for Mean Sea Level.

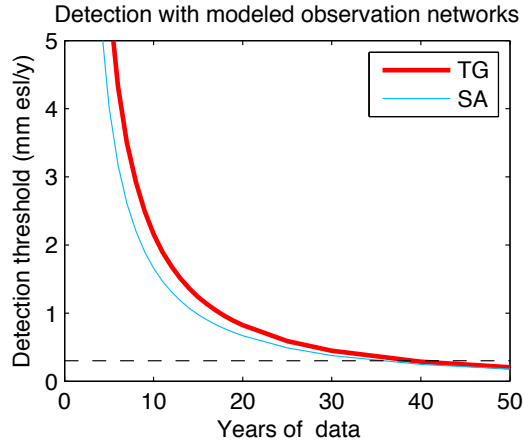


FIGURE S3. Detection thresholds for tide gauge (TG) and satellite altimetry (SA) observations. The dashed line marks the median estimate of current melt rate.

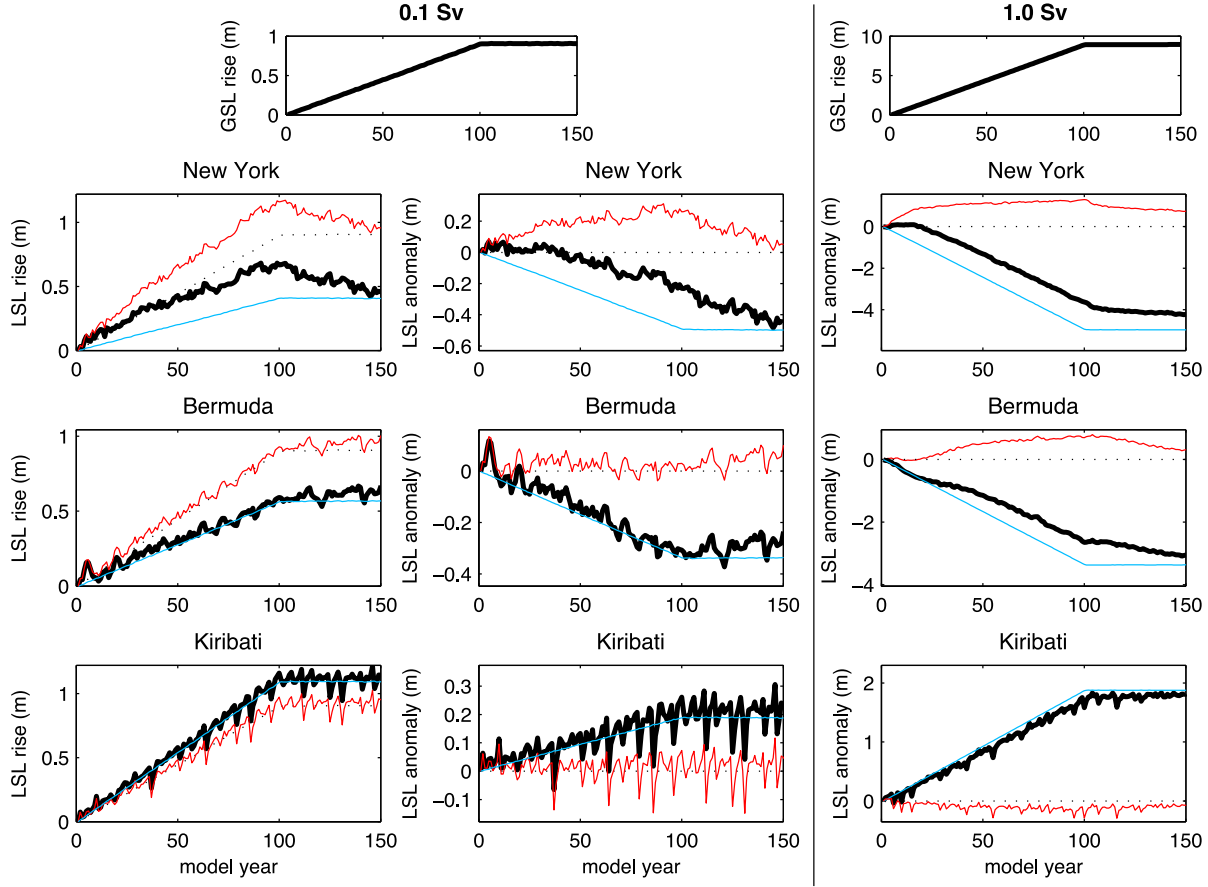


FIGURE S4. LSL rise (left column) or anomaly (center and right columns) including dynamic (red), SE (green) or both dynamic and SE effects (black) at New York City, Bermuda, and Kiribati in the 0.1 Sv (left and center) and 1.0 Sv (right) runs. Top panels and the dotted line in the left column show GSL for each run.

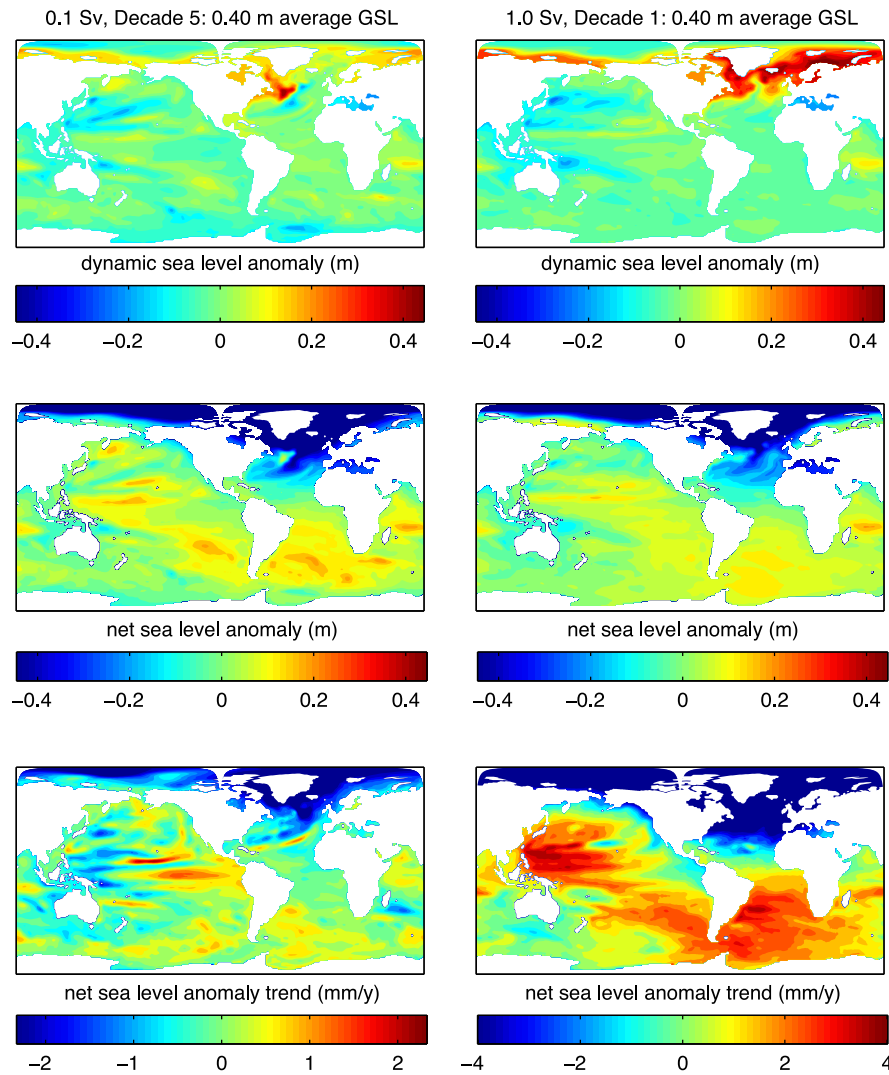


FIGURE S5. Maps of DSL anomaly (top), net dynamic plus SE LSL anomaly (middle), and trend in net anomaly (bottom), averaged over the fifth decade of the 0.1 Sv run (left) and the first decade of the 1.0 Sv run (right). The mean GSL rise is the same in both runs; comparison of the left and right columns reveals the effects of melt rate. LSL anomaly refers to the difference between LSL and GSL.

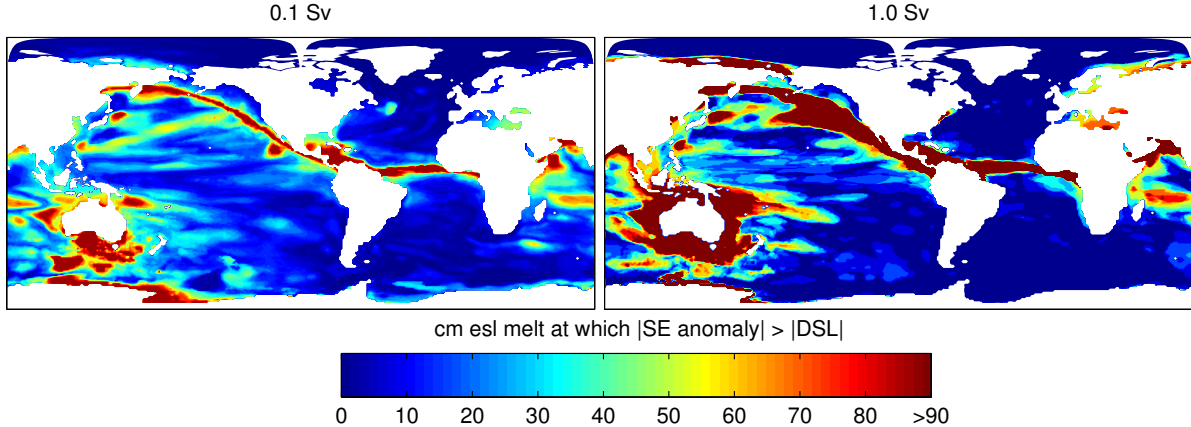


FIGURE S6. Level of total melt at which the amplitude of the SE LSL anomaly first begins to exceed the amplitude of the DSL anomaly in the 0.1 Sv (left) and 1.0 Sv (right) runs. The white triangular masked regions in the north are plotting artifacts arising from the non-spherical Arctic Ocean coordinate grid.

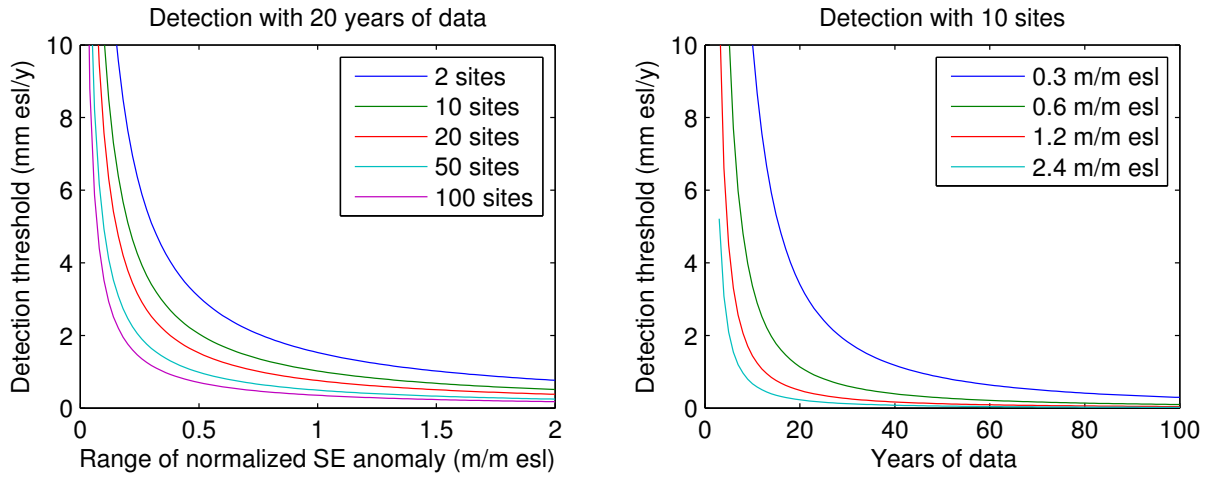


FIGURE S7. Detection thresholds for ice sheet melt at different static equilibrium anomaly ranges, density of observation sites, and years of data, assuming no year-to-year or site-to-site correlation of variability.